ACS Photonics

pubs.acs.org/journal/apchd5

Article

Short-Wave Infrared Confocal Fluorescence Imaging of Deep Mouse Brain with a Superconducting Nanowire Single-Photon Detector

Fei Xia,* Monique Gevers, Andreas Fognini, Aaron T. Mok, Bo Li, Najva Akbari, Iman Esmaeil Zadeh, Jessie Qin-Dregely, and Chris Xu

Cite This: *ACS Photonics* 2021, 8, 2800–2810

Read Online

ACCESS | Metrics & More | Article Recommendations | Supporting Information

ABSTRACT: Optical microscopy is a valuable tool for *in vivo* monitoring of biological structures and functions because of its noninvasiveness. However, imaging deep into biological tissues is challenging due to the scattering and absorption of light. Previous research has shown that the two optimal wavelength windows for high-resolution deep mouse brain imaging are around 1300 and 1700 nm. However, one-photon fluorescence imaging in the wavelength region has been highly challenging due to the poor detection efficiency of currently available detectors. To fully utilize this wavelength advantage, we demonstrated here one-photon confocal fluorescence imaging of deep mouse brains with an excitation wavelength of 1310 nm and an emission wavelength within the 1700 nm window. Fluorescence emission at 1700 nm was detected by a custom-built superconducting nanowire single-photon detector (SNSPD) optimized for detection between 1600 nm and 2000 nm with low detection noise and high detection efficiency. With the PEGylated quantum dots and SNSPD both positioned at the optimal imaging window for deep tissue penetration, we demonstrated *in vivo* one-photon confocal fluorescence imaging at approximately 1.7 mm below the surface of the mouse brain, through the entire cortical column and into the hippocampus region with a low-cost continuous-wave laser source and low excitation power. We further discussed the significance of the staining inhomogeneity in determining the depth limit of one-photon confocal fluorescence imaging. Our work may motivate the further development of long wavelength fluorescent probes, and inspire innovations in high-efficiency, high-gain, and low-noise long wavelength detectors for biological imaging.

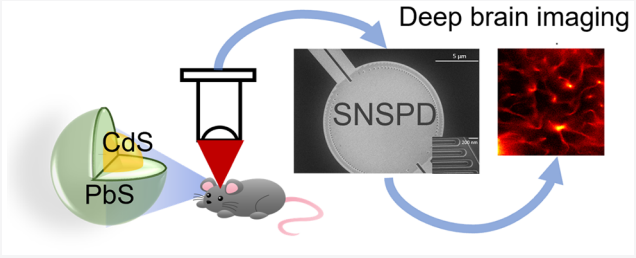

KEYWORDS: *confocal microscopy, deep brain imaging, short-wave infrared region, quantum dots, superconducting nanowire single-photon detector*

Optical microscopy is a valuable tool for noninvasive, high-spatial-resolution imaging of biological processes. Deep imaging at the cellular level within a living biological system is necessary for studying cell−cell interactions in their natural environment. However, due to the strong scattering and absorption of light by biological tissues, deep imaging with high spatial resolution has been challenging. In the last several decades, there were tremendous efforts in exploring various possibilities to push the depth limit of optical microscopy.[1−3] While photoacoustic imaging[4] and diffusive optical tomography[5,6] can access depths at a few millimeters to centimeters, they suffer significantly from low spatial resolutions because of the inherent trade-off between resolution and depth.

For imaging applications that require high spatial resolution, for example, cellular resolution *in vivo* imaging of brains in neuroscience research, the imaging depth is limited to the single-scattering or limited multiple-scattering regimes, and the preservation of ballistic photons and the rejection of scattered photons become essential. Imaging modalities such as multiphoton microscopy (MPM),[7,8] confocal microscopy,[9] and optical coherence tomography/microscopy (OCT/OCM) have been developed that rely on, respectively, nonlinear excitation, confocal gating, and coherence gating[2] to select the signal generated by the ballistic photons to form high-resolution images at depth. Multiphoton and confocal fluorescence microscopy is advantageous because various fluorescence labeling techniques, together with genetic targeting, allow imaging with high specificity. Previous reports of imaging mouse brains *in vivo* with two-photon[10−13] and three-photon microscopy[8,14,15] at depths beyond 1 mm leveraged the optimal wavelength windows for deep tissue penetration at 1300 and 1700 nm. These windows were determined by considering the combined effects of scattering and absorption of ballistic photons in brain tissues *in vivo*.[8,16] On the other hand, one-photon confocal fluorescence

Received: July 7, 2021
Published: September 2, 2021

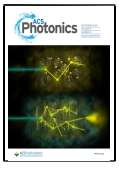

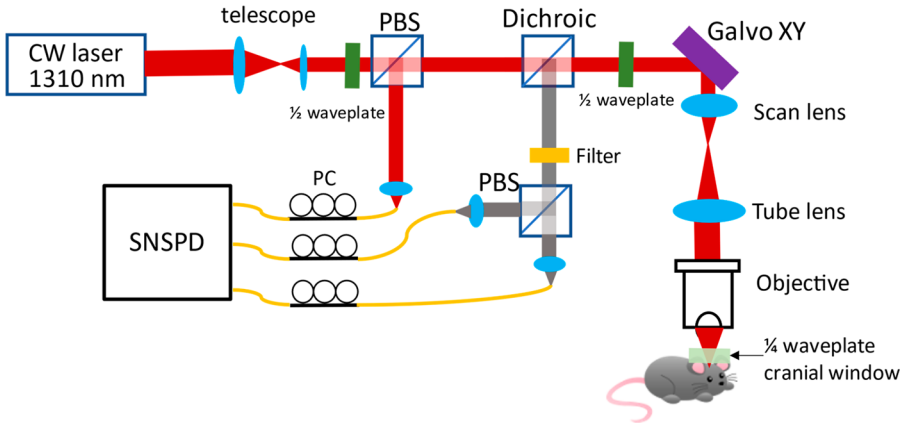

Figure 1. Imaging setup: PBS, polarizing beam splitter; PC, polarization controller; SNSPD, superconducting nanowire single-photon detector. The focal lengths for the scan lens and the tube lens are 35 and 200 mm, respectively. See Methods for more details.

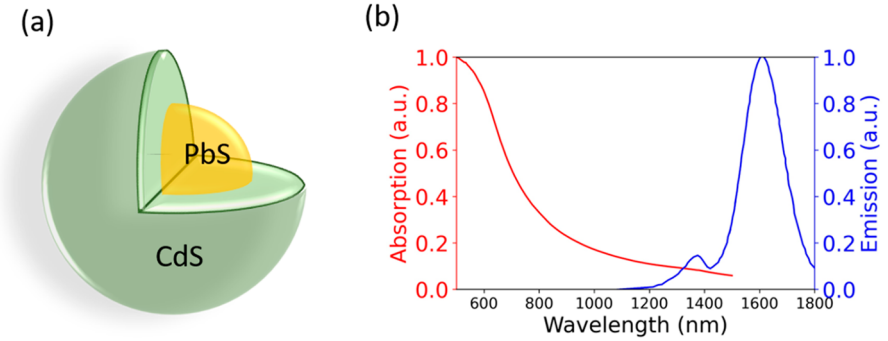

Figure 2. PbS/CdS quantum dot. (a) Schematic structure of the PbS/CdS quantum dot and (b) the absorption and emission spectra of the PbS/CdS quantum dot.

microscopy can provide three-dimensionally resolved imaging capabilities and is still widely used in many biology laboratories. However, confocal imaging depth is often limited due to its short excitation and fluorescence emission wavelengths (typically within the visible light spectrum).[17] Therefore, one-photon confocal fluorescence imaging has only been widely applied to transparent samples such as cleared brain tissues[18,19] or superficial regions of scattering tissue.[20]

In this paper, we aim to push the limit of penetration depth of one-photon confocal fluorescence microscopy in scattering tissue. To take full advantage of the tissue penetration capability of long-wavelength light, we positioned both the excitation and the fluorescence emission wavelengths within the optimal spectral windows for high-spatial-resolution deep brain imaging. We combined PbS/CdS quantum dots (excitation wavelength of 1310 nm and fluorescence emission wavelengths >1600 nm) with the custom-built superconducting nanowire single-photon detectors (SNSPDs) for detection between 1300 and 2000 nm (Figure 1), within short-wave infrared region (SWIR, 1000−2500 nm). We achieved *in vivo* confocal fluorescence microscopy of adult mouse brain vasculature at approximately 1.7 mm depth by using a simple, low-power CW laser for excitation. The long-wavelength confocal microscopy method demonstrated in this paper is robust and straightforward and achieves high spatial resolutions at depths comparable to long wavelength MPM and OCM, which is 3−4 times deeper than previously reported for confocal fluorescence imaging using excitation wavelengths in the visible range. Results obtained in this work shed light on the depth limit of one-photon confocal fluorescence microscopy, advance our understanding of deep tissue microscopy, and may inspire further development of long wavelength fluorophores and detectors.

RESULTS AND DISCUSSIONS

Characterization of the Labeling Agent: PbS/CdS Quantum Dots. One major challenge for one-photon fluorescence imaging at the long-wavelength windows is the availability of long wavelength fluorophores. The most promising options currently are nanomaterials such as carbon nanotubes (CNT)[21] and quantum dots,[22,23] which can have long-wavelength excitation and emission in the short-wave infrared region (1100−1700 nm) by tuning both their sizes and material compositions.[24]

Despite the wide availability of raw nanomaterials, most of them are toxic or insoluble in water. Therefore, surface modifications are necessary to make such materials biocompatible for *in vivo* imaging applications.[25] While probes, such as CNTs, can be engineered to emit long wavelengths, their applications to biological imaging are largely limited to photoluminescence below 1500 nm.[26] If bright probes with a longer emission wavelength are available and biocompatible, they could also be used in imaging the deep mouse brain. Taking into account the brightness, emission wavelength, commercial availability, and biocompatibility, we chose PbS/CdS quantum dots (IR-iNP, Nirmidas Biotech, Inc.)[22] with the emission wavelength (Figure 2b, emission data obtained from the previous work[22]) in the 1700 nm window. The absorption spectrum is measured by a spectrometer (UV−vis-NIR spectrometer, Shimadzu Corp.). The size of the quantum

https://doi.org/10.1021/acsphotonics.1c01018
ACS Photonics 2021, 8, 2800−2810

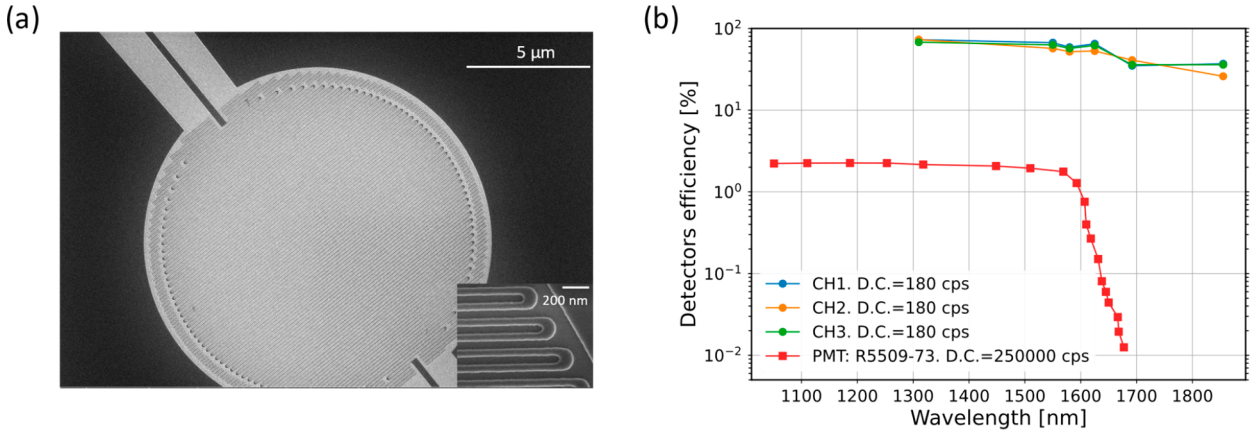

Figure 3. SWIR superconducting nanowire single-photon detector. (a) Scanning electron microscope (SEM) micrograph of a representative meandering nanowire structure. Inset shows the close-up view of the meander nanowires. (b) Measured detector quantum efficiency of the three channels used as a function of wavelengths (circles). The legend also shows the measured dark counts (DC. for each detector at its critical current (i.e., the maximum current that a superconducting wire can carry with zero resistance). For comparison, we also plot the quantum efficiency of a typical InP/InGaAs PMT (squares, R5509-73, Hamamatsu).

dots is ∼20 nm, and they are functionalized with amine groups (NH_2) and PEGylated to make them soluble in aqueous solutions and to improve their biocompatibility. The advantage of these quantum dots is that they are excitable over a wide range of wavelengths, including 1300 nm for deep tissue penetration.

In this work we demonstrated the use of quantum dots for *in vivo* deep imaging of brain vasculature. The uniform labeling of brain vasculature is useful for studying the depth limit of confocal fluorescence microscopy in the mouse brain. On the other hand, imaging the brain vasculature is important for the biological studies of the vasculature topology and blood flow.[27,28] The long wavelength quantum dots are also appealing for applications in drug delivery,[29] biological sensing,[30] and cancer diagnosis[29] when noninvasive probing of deep tissue is required.

High-Sensitivity, Low Noise Superconducting Single-Photon Nanowire SWIR Detector. Another major challenge for one-photon fluorescence imaging at the long-wavelength windows is the lack of high gain, low noise, and high efficiency detectors for detection of the fluorescence. Previous one-photon imaging at the long-wavelength windows[22,31] were all limited to detection wavelengths of less than 1650 nm because of the spectral response of the InGaAs photodiodes or photomultiplier tubes (PMTs). In addition, for low-light level detection, such as detection of the fluorescence, a detector with high quantum efficiency, low dark counts, and high gain is required. Existing detectors such as InGaAs-based PMTs, while having high gain, suffer from low quantum efficiency (typically less than 2.5%) and high dark counts (∼10^5 counts/s).

We customized a SNSPD system for our specific application. The detector has an optimized spectral response between 1600 nm and 2000 nm, a high quantum efficiency (65% at 1625 nm and 36% at 1855 nm), and dark counts <200 counts per second at the operating current in our experiment (see Figure S1(a) for dark counts vs operating current). SNSPDs were previously shown to achieve high detection efficiencies (>90%) in the near-infrared range (780−1000 nm)[32,33] and the telecom bands (1300−1600 nm).[34−36] To achieve a high detection efficiency in the 1300−2000 nm range, several factors were optimized: the NbTiN superconducting film composition, the geometry of the superconducting nanowires (as shown in Figure 3a), and the optical cavity formed by a Au mirror and SiO_2 spacer underneath the superconducting film. Although mid-infrared detectors have been demonstrated for light with wavelengths ranging from 1 to 5 μm[37,38] or even 10 μm,[39] these demonstrations either showed a saturated internal efficiency or demonstrated a limited detection efficiency.[40] Moreover, the materials used in most of these demonstrations (apart from[40]) required operation below the base temperature of conventional Gifford−McMahon cryo-coolers, making the development of a compact microscopy system much more difficult. To the best of our knowledge, this is the first demonstration of a wideband SNSPD in this wavelength range of 1300−2000 nm.

Previously, biological imaging in the SWIR range uses the InGaAs PMT[41] or camera[23] as the detector. We compared the detection efficiency measured at different wavelengths for all three channels in the SNSPD system used for this work with a typical InGaAs PMT within the same wavelength range (Figure 3b). The detection efficiency of the SNSPD is at least 50× higher than that of an InGaAs PMT beyond 1600 nm. Since the SNSPD is a fiber-coupled system, we also compared the performance of two different optical fiber types (SMF28 and PM2000) for coupling with the SNSPDs. Since PM2000 fibers guide longer wavelengths much better than SMF28 fibers, more background from blackbody radiation can couple to the SNSPDs using PM2000. This results in higher dark counts rate, with >10000 counts per second (cps) for PM2000 and <200 cps for SMF28 (Figure S1(b)). Hence, we chose SMF28 to couple to the SNSPD and kept the optical fibers short in this experiment (approximately 2 m) to minimize the transmission loss of the fluorescence signal in the SMF28 optical fibers.

***In Vivo* Deep Imaging of Adult Mouse Brain.** For *in vivo* mouse brain imaging, imaging sessions were conducted immediately after the craniotomy. The mouse preparation is described in detail in the Methods section. The mouse is head-fixed and anesthetized during imaging. The cranial window is centered at 2.2 mm lateral and 2 mm caudal from the bregma point. PbS/CdS quantum dots were retro-orbitally injected into the mouse. We acquired images with a pixel dwell time of 3.8 μs at 512 × 512 pixels/frame. Data were acquired within

https://doi.org/10.1021/acsphotonics.1c01018
ACS Photonics 2021, 8, 2800−2810

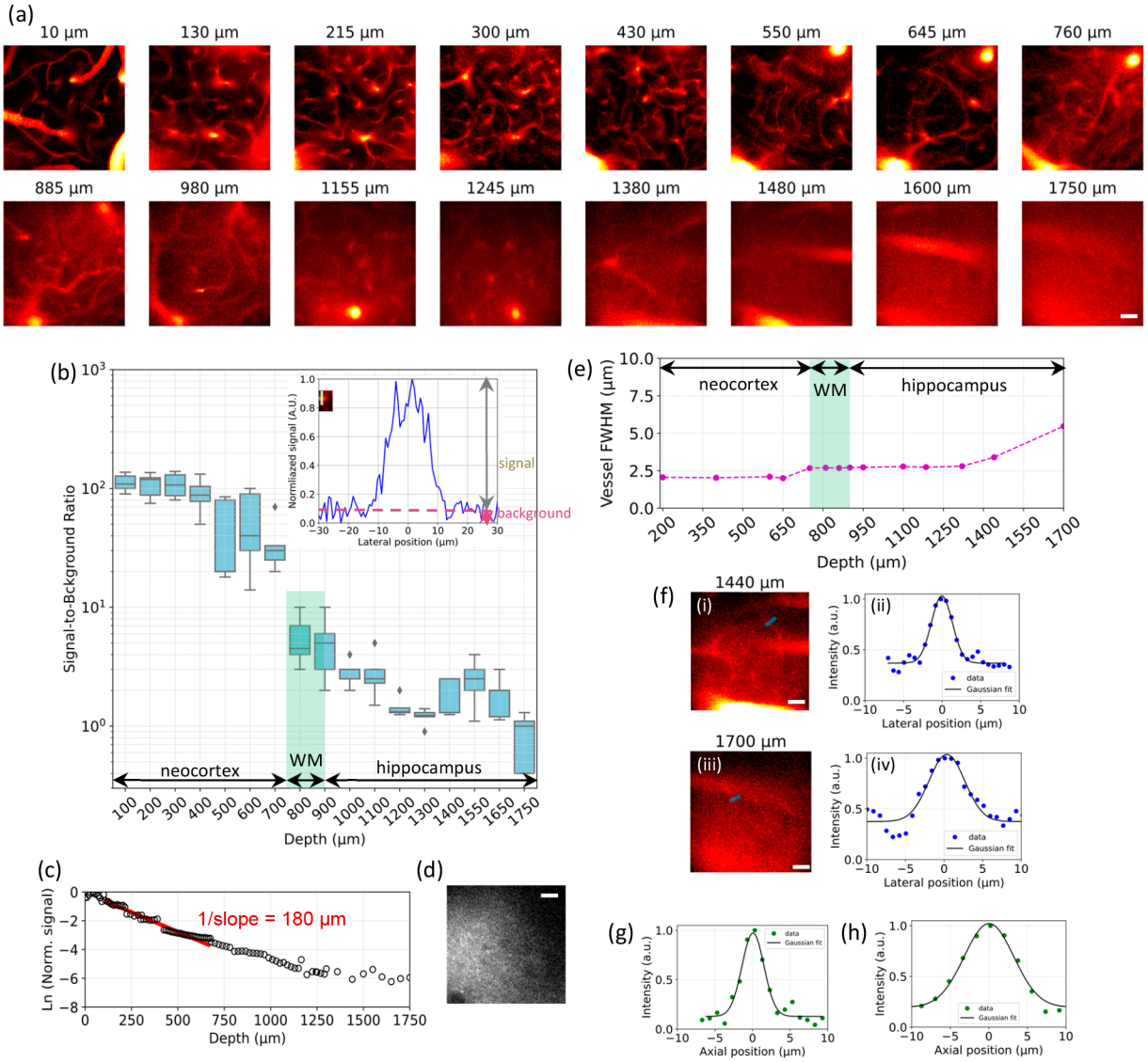

Figure 4. (a) *In vivo* imaging of an adult mouse brain vasculature at various depths with PbS/CdS quantum dots. The scale bar is 50 μm. (b) The signal-to-background ratio (SBR) as a function of imaging depth. The inset in (b) shows an example (at ~500 μm depth) of the SBR calculation where SBR = (total fluorescence − background)/background. The white matter (WM) region of the mouse brain is indicated in green. (c) Fluorescence signal as a function of imaging depth. The fluorescence signal strength at a particular depth is represented by the average value of the brightest 1% of pixels in the x−y image at that depth. The signal is normalized to the signal at the surface of the brain, and is plotted on a logarithmic scale. For the first 400 μm, the fluorescence signal attenuation length (i.e., the depth at which the fluorescence signal is reduced by a factor of e) is approximately 180 μm. (d) White matter image from the reflectance confocal channel at ~750 μm, scale bar is 50 μm. (e) The upper bound of lateral spatial resolution, as defined by the minimum lateral vessel full-width at half-maximum (fwhm) at various depths. The white matter (WM) region is indicated in green. (f) (ii) and (iv) are the lateral intensity profiles of capillaries along the blue lines at the depth of 1440 μm (i) and 1700 μm (iii) with the Gaussian fit (black line) showing the fwhm of 3.3 and 5.5 μm, respectively. The scale bar is 50 μm. (g, h) Axial intensity profile of a capillary at the depth of ~330 μm (g) and 1260 μm (h) with the Gaussian fit (black line) showing the fwhm of 3.4 and 8.4 μm, respectively.

the middle 80% of the scan path of the fast axis, leading to an image acquisition rate of 1 frame per second (fps). Image acquisition for the z-stack progressed from the deepest point to the surface. The excitation power was adjusted to achieve approximately the same signal level at various depths for a constant frame rate of 1 fps and to ensure no excitation saturation (i.e., ground state depletion) occurred. For depths beyond 1.2 mm, the maximum power of approximately 25 mW at the brain surface was used. Imaging integration time was then increased to maintain reasonable signal-to-noise ratios (SNRs) for imaging depth >1.2 mm. At the deepest imaging depth of ~1.7 mm, the integration time was approximately 50 s per frame. Since the mouse is head-fixed and anesthetized, animal motion caused by the heartbeat does not appear to impact the image acquisition even with an integration time of 50 s per frame.

We demonstrated x−y images of the cortical vasculature of the mouse through the somatosensory cortex with the same magnification (Figure 4a). An imaging depth of ~1.7 mm was achieved through the white matter (Figure 4d), significantly extending the previous depth of ~0.4 mm for *in vivo* confocal fluorescence imaging in adult mouse brains with excitation at 400−600 nm[20] or ~0.8 mm with excitation at 810 nm.[31] The images shown at beyond 1 mm depth are in the hippocampus

https://doi.org/10.1021/acsphotonics.1c01018
ACS Photonics 2021, 8, 2800−2810

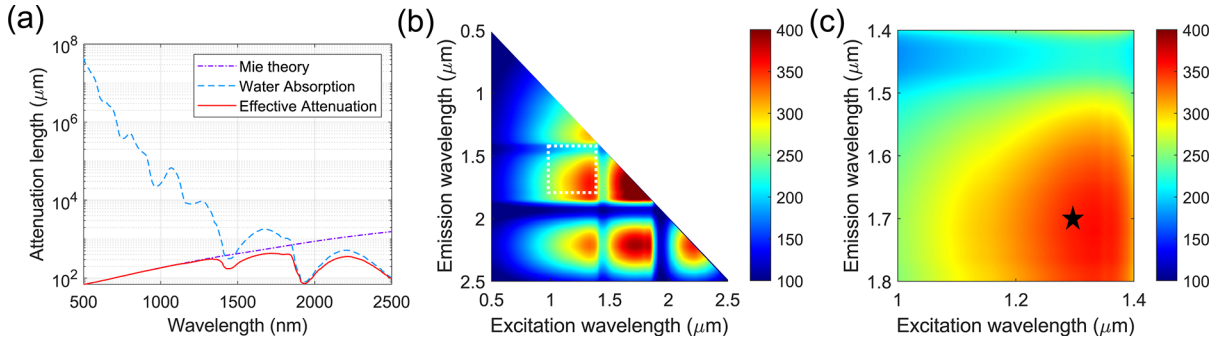

Figure 5. Wavelength selection for deep mouse brain confocal imaging. (a) The calculated effective attenuation length of ballistic photons as a function of wavelengths for mouse brains.[8] (b) The calculated signal attenuation length for a confocal system with a small pinhole. Excitation and emission wavelengths are scanned from 0.5 to 2.5 μm. (c) Zoomed-in version of the region indicated by the box in white dashed line in (b). The color bar has units of μm. The star in (c), with excitation in the 1.3 μm window and emission in the 1.7 μm window, indicates the experimental parameters used in our experiments.

region of the mouse brain, where we observed some large blood vessels, likely to be the arteries or veins, typically tens to a few hundreds of microns diameter in size. Similar large features were also observed in previous three-photon deep imaging works.[42] The bright round dots observed in the images are the blood vessels oriented perpendicular to the cranial window. They are brighter because the collected fluorescence signal is a volume integral of the effective confocal focal volume. The images at 1480 and 1600 μm depth mainly capture a blood vessel with a large diameter imaged at various depths. We observed different small features in the image at 1440 nm and 1700 μm depth.

The fluorescence imaging depth limit is defined as the depth where the signal-to-background ratio (SBR) equals one, which has long been used in multiphoton fluorescence microscopy.[43] To be consistent with previous studies, we used the same criteria (i.e., the depth where SBR = 1) to determine the depth limit for confocal fluorescence microscopy. To quantify the SBR, we plotted the intensity line profiles across lateral blood vessels (Figure 4b). The peak value of the line profile is the sum of the signal from the focal volume and the out-of-focus background, which can be estimated by the intensity of the regions immediately outside the vessel. The SBR measurement is illustrated in the inset in Figure 4b, where SBR = (total fluorescence − background)/background. The SBR decreases with imaging depth, and at the depth at 1.75 mm the SBR was close to one. Compared to 980 and 1060 nm, the absorption at 1300 nm is only 2 to 3 times lower, which means the signal strength is 2 to 3 times lower using 1300 nm excitation. On the other hand, the ballistic photon attenuation length at 1300 nm is ∼1.5 times longer than that at ∼1000 nm. At 1.5 mm imaging depth, the signal strength at 1300 nm is therefore estimated to be ∼18−27 times stronger than that at ∼1000 nm considering ballistic photons collection in the confocal detection and assuming the same power at the sample surface. Our results clearly show that confocal fluorescence *in vivo* imaging with excitation at 1310 nm and emission at >1600 nm can penetrate through the entire cortical layer of the mouse brain. In Figure 4c, we show the detected fluorescence signal as a function of imaging depth. For the first 400 μm, the fluorescence signal attenuation length (i.e., the depth at which the fluorescence signal is reduced by a factor of e) was approximately 180 μm. We further quantified the imaging resolution in the mouse brain.

To evaluate the lateral resolution, we used the smallest blood vessels in each image frame, establishing an upper bound estimation for the lateral resolution (Figure 4e). The fwhm's of the lateral line profiles for capillaries at the depths of 1440 and 1700 μm are 3.3 and 5.5 μm, respectively (Figure 4f). We also measured the axial resolution. The fwhm of the axial intensity profile of a small capillary at the depth of ∼330 μm is ∼3.4 μm (Figure 4g). Our data showed that the lateral resolution degrades significantly below the white matter, and reached a value of ∼5.5 μm at a depth of ∼1.7 mm (with axial resolution degrades to 8.4 μm at ∼1260 μm in Figure 4h). This result implies that in addition to the degrading SBR, optical aberrations are also present, particularly for depth beyond the external capsule (i.e., >1 mm). Therefore, the image contrast below the white matter is poor. Such a situation is similar to what was observed in through-skull two-photon imaging[44] and long wavelength two-photon imaging below the white matter,[11] where the degradation of the point spread function reduced the image contrast.

Wavelength Selection for Deep Mouse Brain Imaging. Ballistic photons attenuate exponentially as a function of imaging depth in scattering and absorbing tissues.[45] The rate of such decay is determined by the effective attenuation length (l_e) of the tissue, which is derived from the scattering mean-free path (l_s) and the absorption length (l_a) of the tissue, where $\frac{1}{l_e} = \frac{1}{l_a} + \frac{1}{l_s}$. The theoretical model combining Mie scattering and water absorption,[8] as shown in Figure 5a, indicates that longer excitation wavelengths within the optimal imaging windows (i.e., the 1300 and 1700 nm windows) have longer attenuation lengths and can therefore reach larger imaging depths.

Previously, the impact of the emission wavelength on multiphoton imaging depth was discussed, and it was found that the emission wavelength has a limited impact on MPM. This is because typical MPM systems operate in a widefield collection mode, where scattered fluorescence photons are also efficiently collected.[46] The imaging depth in MPM is hence mostly determined by the excitation wavelength. In one-photon confocal fluorescence microscopy, however, the confocal pinhole preferentially selects ballistic photons for fluorescence detection. Therefore, in one-photon confocal fluorescence imaging, the emission wavelength has the same impact as the excitation wavelength on imaging depth, and the fluorescence signal attenuates as $e^{-z/l_{ex}} \times e^{-z/l_{em}}$, where l_{ex} and

https://doi.org/10.1021/acsphotonics.1c01018
ACS Photonics 2021, 8, 2800−2810

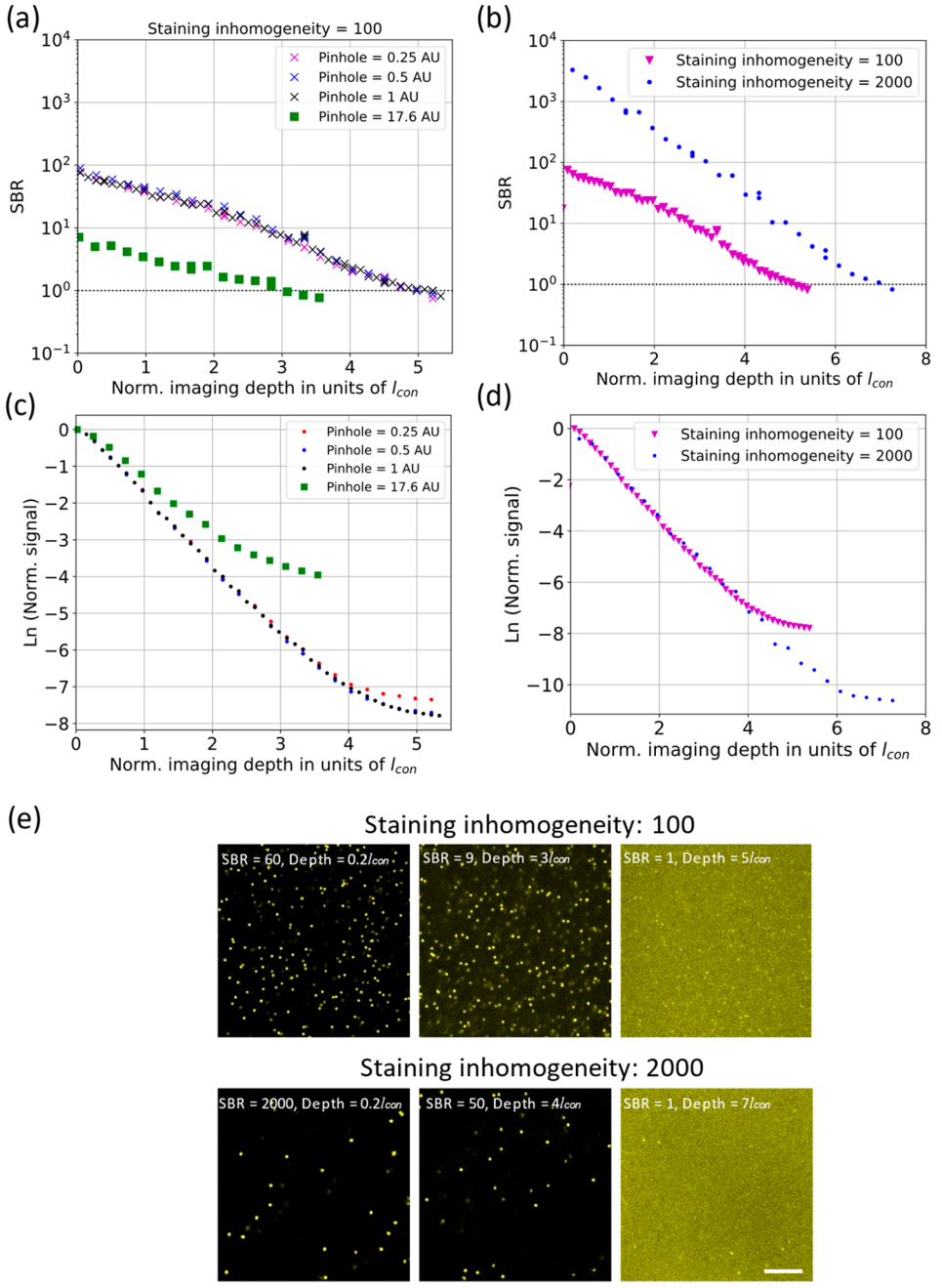

Figure 6. (a) SBR as a function of imaging depth for various confocal pinhole sizes. The depth is normalized by the l_{con} in (a)−(d) and AU is an Airy unit. (b) SBR as a function of imaging depth with two different staining inhomogeneities. (c) Signal as a function of imaging depth with various confocal pinhole sizes. The signal is normalized to the signal at the sample surface. (d) Signal as a function of imaging depth with two different staining inhomogeneities. (e) Images at various normalized depths for the staining inhomogeneities of 100 (top) and 2000 (bottom). The SBRs are indicated in the images. Scale bar: 30 μm.

l_{em} are the effective attenuation lengths of the tissue at the excitation and emission wavelength, respectively, and z is the imaging depth. To normalize the imaging depth, instead of using the length scale that corresponds to the decay of the fluorescence signal as a function of imaging depth, here we will use the length scale that reflects the optical property of the tissue at the excitation and emission wavelength. By averaging the attenuation coefficients in the excitation (l_{ex}^{-1}) and the emission paths (l_{em}^{-1}), that is, $\frac{1}{2}(l_{ex}^{-1} + l_{em}^{-1})$, we can define the confocal imaging attenuation length (l_{con}) as $l_{con} = \frac{2}{\frac{1}{l_{ex}} + \frac{1}{l_{em}}}$ (Figure 5b,c). Such a definition is also consistent with previous conventions in MPM[8,11] and reflectance confocal imaging.[2,47] In principle, l_{con} is maximized when $l_{ex} = l_{em}$ and l_{ex} is at its maximum, as seen in Figure 5b. This corresponds to confocal reflectance imaging at the optimal imaging window of ∼1700 nm, as shown in a previous paper.[41]

For confocal fluorescence imaging, and taking into account the Stokes shift, Figure 5b,c shows that the l_{con} reached the maximum values with three pairs of excitation and emission wavelengths: (1) excitation in the 1300 nm window and emission in the 1700 nm window (this work), (2) excitation in the 1700 nm window and emission in the 2200 nm window,

https://doi.org/10.1021/acsphotonics.1c01018
ACS Photonics 2021, 8, 2800−2810

and (3) both excitation and emission in the 1700 window. Therefore, in addition to the results shown here, there are additional opportunities for long-wavelength confocal fluorescence imaging if appropriate fluorescent labels exist. We note that the considerations for the wavelength selections discussed here are also applicable to nonlinear excitations where two or more wavelengths are employed for excitation such as nondegenerate two-photon excitation,[48] stimulated Raman scattering,[49] and pump−probe imaging.[50,51]

With the estimated confocal signal attenuation length, we can determine the absolute imaging depth limit of fluorescence confocal microscopy in the following section.

Experimental Investigation of the Depth Limit of One-Photon Confocal Fluorescence Imaging. Confocal fluorescence microscopy has long seen limited use in deep tissue imaging due to its excitation wavelength being typically in the visible spectrum. Therefore, the imaging depth limit of confocal fluorescence microscopy has not been investigated thoroughly, unlike in MPM. Discussions of the imaging depth limit of confocal microscopy have further been limited to confocal reflectance modes, in comparison with OCT/OCM,[9,47,52,53] mainly focused on the parameters such as the anisotropy factor and the numerical aperture (NA). However, the image contrast in confocal reflectance imaging comes from anywhere that has backscattering, while that of confocal fluorescence imaging comes only from the fluorescence-labeled regions. To discuss the imaging depth limit of confocal fluorescence imaging in a scattering medium at high-spatial resolutions, we need to specifically take into account staining inhomogeneity (defined as the inverse of the volume fraction of the sample that are labeled), a factor that was known to be essential in MPM[54] but not discussed in previous work on confocal imaging depth limit. The staining inhomogeneity can vary dramatically in different applications. For example, the staining inhomogeneity is approximately 50 when imaging the mouse brain vasculature.[10,55,56] On the other hand, the staining inhomogeneity is highly varied when imaging neurons in a transgenic mouse brain.[10] Therefore, similar to MPM, the staining inhomogeneity is an essential parameter for determining the imaging depth limit of one-photon confocal fluorescence imaging.

Here we experimentally investigate the depth limit of confocal fluorescence imaging at high-spatial resolutions in a tissue phantom that exhibits similar scattering properties of the mouse brain. We varied the staining inhomogeneity and examined the effects of the pinhole size on imaging depth using a commercial confocal fluorescence microscope (see the Methods section). The depth limit was defined by the condition SBR = 1, similar to MPM. Fluorescence originating from the beads is determined by the brightness at the center of the fluorescent beads (total fluorescence) minus the brightness of the area that does not contain beads (i.e., out-of-focus background). This is the same method used in previous SBR measurements in MPM.[54] We found that the imaging depth limit does not change significantly when the pinhole size is small (~1 Airy unit or less). When the pinhole size is much larger (Figure 6a,c), the SBR and, therefore, the imaging depth limit degrade significantly. For a staining inhomogeneity of 100, we found the depth limit of $\sim 5l_{con}$ with the confocal pinhole at 1 Airy unit or less, and $\sim 2.8l_{con}$ with the confocal pinhole at 17.6 Airy units (the largest pinhole size we can reach with the LSM880 confocal microscope, see Methods). The experimental data on the staining inhomogeneity of beads are in good agreement with data of the mouse brain vasculature (staining inhomogeneity of ~50 in cortex and thalamus[55] and ~100 in the hippocampus[55,56]), with both imaging results showing the depth limits at $\sim 5l_{con}$. When varying the fluorescence staining inhomogeneity, the imaging depth limit changes (Figure 6b,d). For the same pinhole size (1 Airy unit; also 1 Airy unit is used in the *in vivo* imaging system), the depth limit increases from $\sim 5l_{con}$ for a staining inhomogeneity of 100 (Figure 6a,c,e) to $\sim 7l_{con}$ for a staining inhomogeneity of 2000 (Figure 6b,d,e). This indicates that the larger the staining inhomogeneity, the deeper confocal fluorescence microscopy can reach. Note that high staining inhomogeneity is practical as many biologists regularly locally label the fluorescence for visualizing processes in a specific region of interest by techniques such as localized injection for *in vivo* observation. Using the estimated confocal signal attenuation length we obtained in the previous section, we are able to estimate the absolute depth limit for confocal fluorescence imaging of the mouse brain *in vivo*. In the case of staining inhomogeneity of ~100, which is close to the vasculature labeling in the brain, an absolute depth limit of about ~1.77 mm is calculated ($\sim 5l_{con}$, where $l_{con} \sim 354$ μm from the simulation in Figure 5c when positioning the excitation wavelength at ~1300 nm and the emission wavelength at ~1700 nm). This theoretical prediction is close to our experimental result of a depth limit of 1.7 mm.

The dependence of the depth limit on staining inhomogeneity for one-photon confocal fluorescence imaging is similar to that in two-photon microscopy.[54] Indeed, assuming the excitation and emission wavelengths of confocal fluorescence imaging is similar to the excitation wavelength of two-photon microscopy, our data indicate that, based on the SBR, one-photon confocal imaging can achieve the same penetration depth as two-photon microscopy.

Imaging with close to diffraction-limited spatial resolution deep within scattering tissues requires imaging with ballistic photons, unless scattering compensation techniques are employed.[57,58] Common techniques of ballistic photon imaging include wide-field, confocal, OCT/OCM, and multiphoton microscopy. The imaging depth of these techniques are mainly limited by multiple-scattering photons. Since the scattering and absorption lengths of biological tissues are strongly wavelength-dependent, the absolute imaging depth limit depends critically on the wavelength used. In addition, for fluorescence imaging, the choice of the imaging wavelength is further constrained by the available fluorophores. Based on the calculations in Figure 5, we can quantify the advantage of the longer emission wavelength. For example, by positioning the emission wavelength at 1700 nm instead of at 1500 nm, with the same excitation wavelength at 1300 nm, an increase of ~80 μm in confocal attenuation lengths (l_{con}) is obtained, which results in $5 \times l_{con} = 400$ μm of increased depth limit in fluorescence confocal imaging. A similar impact of emission wavelength on imaging depth has been experimentally demonstrated in single-photon light-sheet microscopy.[23] While the long-wavelength confocal imaging shown in this paper reached a comparable imaging depth as long-wavelength two-photon imaging and is free of autofluorescence, the requirement of SWIR dyes is a major limitation for long wavelength one-photon imaging since a majority of organic fluorophores and almost all fluorescent proteins require visible or near-IR excitation (i.e., <750 nm). Therefore, in addition to limiting photobleaching and photodamage to the focal plane

https://doi.org/10.1021/acsphotonics.1c01018
ACS Photonics 2021, 8, 2800−2810

and efficient wide-field fluorescence collection with its three-dimensional localized excitation, the advantage of two-photon microscopy for deep tissue imaging when compared to one-photon confocal imaging is mainly due to the compatibility of the long wavelength windows for deep tissue penetration with two-photon excitation of existing fluorophores. If SWIR dyes and proteins were to become widely available for *in vivo* imaging, given the convenience and advantages of one-photon excitation, it would be conceivable that one-photon confocal fluorescence microscopy can play a major role in deep imaging of scattering tissues.

CONCLUSION

In summary, we demonstrate *in vivo* deep-brain confocal fluorescence microscopy with excitation and emission both within the optimal wavelength windows for deep tissue penetration, that is, 1300 and 1700 nm, with a customized SNSPD with high detection efficiency. Our experiments were enabled by the combination of PEGylated PbS/CdS quantum dots and an SNSPD system for detection in the SWIR spectral range. With the optimized wavelength selection, we were able to achieve *in vivo* confocal fluorescence imaging of adult mouse brain vasculature with high spatial resolution at a depth of approximately 1.7 mm, which is 2−4 times deeper than previous one-photon confocal fluorescence imaging results. While SNSPD was available in the past, it was mainly used for quantum optics research. Our work opens a new application area for SNSPD, especially in the spectral region beyond the reach of conventional InGaAs detectors, and the use of SNSPD is essential to achieving the high detection efficiency and low dark counts needed for *in vivo* SWIR fluorescence imaging in biological applications. By experimentally investigating the depth limit of one-photon confocal fluorescence imaging, we further show that the depth limit of confocal fluorescence imaging depends critically on the staining inhomogeneity and, when normalized to the attenuation length, is comparable to that of two-photon imaging. Long wavelength confocal fluorescence imaging, as shown in this paper, can reach similar imaging depths as long wavelength two-photon microscopy. Our work may motivate the further development of long wavelength fluorescent probes that are designed with peak excitation and an emission wavelength within the optimum spectral window for tissue penetration and inspire innovations in high-efficiency, high-gain, and low-noise SWIR detectors that are tailored for biological imaging.

MATERIALS AND METHODS

Short-Wave Infrared Confocal Fluorescence Microscopy Setup. All *in vivo* images were taken with a customized laser scanning microscope with a high numerical aperture objective (Olympus XLPLN25XWMP2, 25×, effective NA ∼ 1.0) and epi-collection of the signal, as shown in Figure 1. The back aperture of the objective was overfilled to make full use of the numerical aperture (NA). The fluorescence signal is separated from the excitation light using a dichroic mirror (DMSP1500R, Thorlabs) and then epi-collected. Since the superconducting nanowire single-photon detector is polarization-sensitive, we split the epi-collected fluorescence signal into two orthogonal polarizations using a polarization beam splitter (PBS) and adjusted the two fiber polarization controllers (FPC562, Thorlabs.) to optimize the detection efficiency. Furthermore, to monitor the reflectance signal from the brain, we set up a confocal reflectance path with a PBS and a cranial window in the form of a $\lambda/4$ waveplate to separate the illumination and backscattered light and to eliminate the spurious back reflection from the various optical elements in the microscope. This technique was introduced in our previous work.[41] We used a continuous-wave (CW) diode laser as the illumination source at 1310 nm (FPL1053P, Thorlabs). The epi-collected light was descanned, long-pass filtered (FELH1500, Thorlabs) and refocused by aspheric lenses into single-mode fibers (SMF-28), which also served as the confocal apertures. The focusing lenses are chosen to match the confocal pinhole so that an effective aperture size of 1 Airy unity is achieved. For analog signal acquisition, signal is lock-in amplified and an additional 240 kHz low pass filter (EF504, Thorlabs) was used before digital sampling. The signal acquisition system displayed shot-noise-limited performance and dark counts of <200 counts per second under actual imaging conditions without laser scanning. Image acquisition and stage control were performed using ScanImage (version 5.6) running in MATLAB (MathWorks 2018a). The SNSPD detector is maintained and operated at ∼2.6K. The current applied to the SNSPD was adjusted based on the signal strength and the required bandwidth. The analog-to-digital conversion was performed by a data acquisition card (NI PCI-6110, National Instruments).

Fabrication of the SNSPD Detector. The fabrication of the SNSPD detector is briefly described here. Through thermal oxidization, a 280−310 nm thick SiO_2 layer was grown on a commercial silicon wafer. The NbTiN thin film was then deposited by cosputtering of Nb and Ti in a plasma of Ar and N_2, as described in our previous work.[59] The meandering nanowire structure was then patterned using electron beam lithography with either XR1541(negative) or AR-P 6200.04 (positive) E-beam resist and reactive ion etching in a plasma of SF_6 and O_2. Similar to the previous work,[36] backside photolithography was aligned to the detector (on the front side), and a two-step deep reactive ion etching (Bosch process) was used to release detector/SiO_2 membrane and fabricate a gold mirror beneath the membrane. Finally, another lithographic step and through-wafer Bosch process were used to fully release the chips from the substrate in a keyhole shape that is compatible with FC fiber mating sleeves.[60]

Animal Preparation and *In Vivo* Adult Mouse Brain Imaging. All animal procedures were performed with the approval of the Cornell Institutional Animal Care and Use Committee (IACUC) and under the guidance of the Cornell Center for Animal Resources and Education.

For the *in vivo* mouse imaging, imaging sessions were conducted immediately after the craniotomy. We used a 5 × 5 mm square-shaped $\lambda/4$-waveplate (WPQ501, Thorlabs) instead of the normal cover-glass as the cranial window, as described in our previous work.[41] This was done to reduce the background in the reflectance signal detection path. We imaged wild-type C57BL/6J mice (8−12 weeks old, n = 3, all male) with 5 mm cranial windows centered at 2.2 mm lateral and 2 mm caudal from the bregma point using PbS/CdS quantum dots retro-orbitally injected into the mice. The injection dose of the PEGlayted PbS/Cds quantum dots depends on the mouse's weight; typically, the dose is the weight times 10 mL/kg. The injection does in our work is ∼0.2 mL. The maximum optical power at the surface of the mouse brain was approximately 25 mW for the deepest imaging. The head-fixed mouse was anesthetized (1−1.5% isoflurane mixed

https://doi.org/10.1021/acsphotonics.1c01018
ACS Photonics 2021, 8, 2800−2810

with oxygen) and placed on a motorized stage (M-285, Sutter Instrument Company) for axial scanning. Deuterium oxide (i.e., heavy water, D_2O) was used as the objective immersion medium to reduce the absorption caused by water (H_2O), particularly at emission wavelengths beyond 1550 nm.[61,62] For depth measurement, the slightly larger index of refraction in the mouse brain (1.35 to 1.43 for the cortex), relative to D_2O (~1.33), results in an underestimate (5−10%) of the actual imaging depth within the tissue because the imaging depths reported here are the raw axial movement of the motorized stage. The images in Figure 4a are median filtered with 1-pixel radius and are in pseudo color for visualization purposes with the top 0.2−0.4% pixels saturated.

Bead Preparation and Confocal Fluorescence Imaging of the Bead Phantom. The bead phantom was prepared with different ratios of yellow−green fluorescent beads (505/515, FluoSpheres Polystyrene Microspheres 1.00 μm, ThermoFisher, Inc.) and polystyrene beads (Polybead Microspheres 1.00 μm, Polysciences, Inc.) embedded in a 1% (w/v) agarose gel (A7174 Sigma-Aldrich). A detailed preparation protocol can also be found in the previous work.[54] The imaging of the bead phantom was performed using a laser scanning confocal microscope (LSM880 Confocal multiphoton upright - u880, Zeiss Inc.) with excitation at 488 nm and detection beyond 500 nm. The phantom attenuation length was characterized by a spectral transmission measurement of a thin slab with known thickness with a spectrometer (Cary 5000 UV−vis-NIR spectrophotometer) and calculated by the transmission at 488 nm and 515 nm (Supplementary section 2 and Figure S2), similar to the previous work[54]

■ ASSOCIATED CONTENT

Supporting Information

The Supporting Information is available free of charge at https://pubs.acs.org/doi/10.1021/acsphotonics.1c01018.

(1) Characterization of the SNSPD; (2) Optical characterization of the scattering bead phantom (PDF)

■ AUTHOR INFORMATION

Corresponding Author

Fei Xia − *School of Applied and Engineering Physics, Cornell University, Ithaca, New York 14853, United States; Meinig School of Biomedical Engineering, Cornell University, Ithaca, New York 14853, United States;* orcid.org/0000-0001-6591-8769; Email: fx43@cornell.edu

Authors

Monique Gevers − *Single Quantum B.V., 2629 JD Delft, The Netherlands*

Andreas Fognini − *Single Quantum B.V., 2629 JD Delft, The Netherlands*

Aaron T. Mok − *School of Applied and Engineering Physics, Cornell University, Ithaca, New York 14853, United States*

Bo Li − *School of Applied and Engineering Physics, Cornell University, Ithaca, New York 14853, United States*

Najva Akbari − *School of Applied and Engineering Physics, Cornell University, Ithaca, New York 14853, United States*

Iman Esmaeil Zadeh − *Single Quantum B.V., 2629 JD Delft, The Netherlands; Optics Research Group, ImPhys Department, Faculty of Applied Sciences, Delft University of Technology, 2628 CJ Delft, The Netherlands*

Jessie Qin-Dregely − *Single Quantum B.V., 2629 JD Delft, The Netherlands*

Chris Xu − *School of Applied and Engineering Physics, Cornell University, Ithaca, New York 14853, United States*

Complete contact information is available at: https://pubs.acs.org/10.1021/acsphotonics.1c01018

Funding

National Science Foundation (DBI-1707312, Cornell NeuroNex Hub). National Institute of Health S10OD018516 funding for the shared Zeiss LSM880 confocal/multiphoton microscope. Single Quantum B.V. acknowledges funding from H2020 SME Instrument: SQP (Grant No. 848827). I.E.Z. and Single Quantum B.V. acknowledge the support from the ATTRACT project funded by the EC under Grant Agreement No. 777222 (PIZZICATO Project, Gisiphod Project, Smil Project, and Inspect Project).

Notes

The authors declare the following competing financial interest(s): The following authors were employed by Single Quantum and may profit financially: M.G., A.F., I.E.Z., and J.Q.-J.

■ ACKNOWLEDGMENTS

The authors thank Dr. Martin Caldarola (Single Quantum Inc.) for technical assistance.

■ REFERENCES

(1) Huang, D.; Swanson, E. A.; Lin, C. P.; Schuman, J. S.; Stinson, W. G.; Chang, W.; Hee, M. R.; Flotte, T.; Gregory, K.; Puliafito, C. a; Flotire, T.; Gregory, K.; Puliafito, C. a; Fujimoto, J. G.; et al. Optical Coherence Tomography. *Science* **1991**, *254* (5035), 1178−1181.

(2) Izatt, J. A.; Hee, M. R.; Owen, G. M.; Swanson, E. A.; Fujimoto, J. G. Optical Coherence Microscopy in Scattering Media. *Opt. Lett.* **1994**, *19* (8), 590−592.

(3) Ntziachristos, V. Going Deeper than Microscopy: The Optical Imaging Frontier in Biology. *Nat. Methods* **2010**, *7* (8), 603−614.

(4) Wang, L. V.; Yao, J. A Practical Guide to Photoacoustic Tomography in the Life Sciences. *Nat. Methods* **2016**, *13* (8), 627−638.

(5) Boas, D.A.; Brooks, D.H.; Miller, E.L.; DiMarzio, C.A.; Kilmer, M.; Gaudette, R.J.; Quan Zhang. Imaging the Body with Diffuse Optical Tomography. *IEEE Signal Process. Mag.* **2001**, *18* (6), 57−75.

(6) Hoshi, Y.; Yamada, Y. Overview of Diffuse Optical Tomography and Its Clinical Applications. *J. Biomed. Opt.* **2016**, *21* (9), 091312.

(7) Denk, W.; Strickler, J. H.; Webb, W. W. Two-Photon Laser Scanning Fluorescence Microscopy. *Science (Washington, DC, U. S.)* **1990**, *248* (4951), 73−76.

(8) Horton, N. G.; Wang, K.; Kobat, D.; Clark, C. G.; Wise, F. W.; Schaffer, C. B.; Xu, C. In Vivo Three-Photon Microscopy of Subcortical Structures within an Intact Mouse Brain. *Nat. Photonics* **2013**, *7* (3), 205.

(9) Schmitt, J. M. M.; Knüttel, A.; Yadlowsky, M. Confocal Microscopy in Turbid Media. *J. Opt. Soc. Am. A* **1994**, *11* (8), 2226.

(10) Wang, T.; Wu, C.; Ouzounov, D. G.; Gu, W.; Xia, F.; Kim, M.; Yang, X.; Warden, M. R.; Xu, C. Quantitative Analysis of 1300-Nm Three-Photon Calcium Imaging in the Mouse Brain. *eLife* **2020**, *9*, 1−22.

(11) Kobat, D.; Horton, N. G.; Xu, C. In Vivo Two-Photon Microscopy to 1.6-Mm Depth in Mouse Cortex. *J. Biomed. Opt.* **2011**, *16* (10), 106014.

(12) Kobat, D.; Durst, M. E.; Nishimura, N.; Wong, A. W.; Schaffer, C. B.; Xu, C. Deep Tissue Multiphoton Microscopy Using Longer Wavelength Excitation. *Opt. Express* **2009**, *17* (16), 13354−13364.

(13) Cheng, H.; Tong, S.; Deng, X.; Li, J.; Qiu, P.; Wang, K. In Vivo Deep-Brain Imaging of Microglia Enabled by Three-Photon Fluorescence Microscopy. *Opt. Lett.* **2020**, *45* (18), 5271.
(14) Ouzounov, D. G.; Wang, T.; Wang, M.; Feng, D. D.; Horton, N. G.; Cruz-Hernández, J. C.; Cheng, Y. T.; Reimer, J.; Tolias, A. S.; Nishimura, N.; Xu, C. In Vivo Three-Photon Imaging of Activity of GCaMP6-Labeled Neurons Deep in Intact Mouse Brain. *Nat. Methods* **2017**. *14*388.
(15) Li, D.; Zhang, H.; Streich, L. L.; Wang, Y.; Lu, P.; Wang, L.; Prevedel, R.; Qian, J. AIE-Nanoparticle Assisted Ultra-Deep Three-Photon Microscopy in the in Vivo Mouse Brain under 1300 Nm Excitation. *Mater. Chem. Front.* **2021**. 5732013208.
(16) Wang, M.; Wu, C.; Sinefeld, D.; Li, B.; Xia, F.; Xu, C. Comparing the Effective Attenuation Lengths for Long Wavelength in Vivo Imaging of the Mouse Brain. *Biomed. Opt. Express* **2018**, *9* (8), 3534.
(17) Pawley, J. Fundamental Limits in Confocal Microscopy. *Handb. Biol. Confocal Microsc.* **1995**, 19−37.
(18) Song, E.; Ahn, Y.; Ahn, J.; Ahn, S.; Kim, C.; Choi, S.; Boutilier, R. M.; Lee, Y.; Kim, P.; Lee, H. Optical Clearing Assisted Confocal Microscopy of Ex Vivo Transgenic Mouse Skin. *Opt. Laser Technol.* **2015**, *73*, 69−76.
(19) Organs, O. I.; Epp, J. R.; Niibori, Y.; Hsiang, H. L.; Mercaldo, V.; Deisseroth, K.; Josselyn, S. a; Frankland, P. W. Optimization of CLARITY for Clearing Whole-Brain. *ENeuro* **2015**, *2* (June), 1−15.
(20) Schain, A. J.; Hill, R. A.; Grutzendler, J. Label-Free in Vivo Imaging of Myelinated Axons in Health and Disease with Spectral Confocal Reflectance Microscopy. *Nat. Med.* **2014**, *20* (4), 443−449.
(21) Wan, H.; Yue, J.; Zhu, S.; Uno, T.; Zhang, X.; Yang, Q.; Yu, K.; Hong, G.; Wang, J.; Li, L.; et al. A Bright Organic NIR-II Nanofluorophore for Three-Dimensional Imaging into Biological Tissues. *Nat. Commun.* **2018**, *9* (1), 1−9.
(22) Zhang, M.; Yue, J.; Cui, R.; Ma, Z.; Wan, H.; Wang, F.; Zhu, S.; Zhou, Y.; Kuang, Y.; Zhong, Y.; Pang, D. W.; Dai, H. Bright Quantum Dots Emitting at ∼ 1,600 Nm in the NIR-IIb Window for Deep Tissue Fluorescence Imaging. *Proc. Natl. Acad. Sci. U. S. A.* **2018**, *115* (26), 6590−6595.
(23) Wang, F.; Wan, H.; Ma, Z.; Zhong, Y.; Sun, Q.; Tian, Y.; Qu, L.; Du, H.; Zhang, M.; Li, L.; Ma, H.; Luo, J.; Liang, Y.; Li, W. J.; Hong, G.; Liu, L.; Dai, H. Light-Sheet Microscopy in the near-Infrared II Window. *Nat. Methods* **2019**, *16* (6), 545−552.
(24) Pisanic, T. R.; Zhang, Y.; Wang, T. H. Quantum Dots in Diagnostics and Detection: Principles and Paradigms. *Analyst* **2014**, *139* (12), 2968−2981.
(25) Kunzmann, A.; Andersson, B.; Thurnherr, T.; Krug, H.; Scheynius, A.; Fadeel, B. Toxicology of Engineered Nanomaterials: Focus on Biocompatibility, Biodistribution and Biodegradation. *Biochim. Biophys. Acta, Gen. Subj.* **2011**, *1810* (3), 361−373.
(26) Paviolo, C.; Cognet, L. Near-Infrared Nanoscopy with Carbon-Based Nanoparticles for the Exploration of the Brain Extracellular Space. *Neurobiol. Dis.* **2021**, *153*, 105328.
(27) Hernandez, J. C. C.; Bracko, O.; Kersbergen, C. J.; Muse, V.; Haft-Javaherian, M.; Berg, M.; Park, L.; Vinarcsik, L. K.; Ivasyk, I.; Rivera, D. Neutrophil Adhesion in Brain Capillaries Reduces Cortical Blood Flow and Impairs Memory Function in Alzheimer's Disease Mouse Models. *Nat. Neurosci.* **2019**, *22* (3), 413−420.
(28) Jia, Y.; Morrison, J. C.; Tokayer, J.; Tan, O.; Lombardi, L.; Baumann, B.; Lu, C. D.; Choi, W.; Fujimoto, J. G.; Huang, D. Quantitative OCT Angiography of Optic Nerve Head Blood Flow. *Biomed. Opt. Express* **2012**, *3* (12), 3127−3137.
(29) Bilan, R.; Nabiev, I.; Sukhanova, A. Quantum Dot-Based Nanotools for Bioimaging, Diagnostics, and Drug Delivery. *ChemBioChem* **2016**, *17* (22), 2103−2114.
(30) Hildebrandt, N.; Spillmann, C. M.; Algar, W. R.; Pons, T.; Stewart, M. H.; Oh, E.; Susumu, K.; Diaz, S. A.; Delehanty, J. B.; Medintz, I. L. Energy Transfer with Semiconductor Quantum Dot Bioconjugates: A Versatile Platform for Biosensing, Energy Harvesting, and Other Developing Applications. *Chem. Rev.* **2017**, *117* (2), 536−711.
(31) Yu, W.; Guo, B.; Zhang, H.; Zhou, J.; Yu, X.; Zhu, L.; Xue, D.; Liu, W.; Sun, X.; Qian, J. NIR-II Fluorescence in Vivo Confocal Microscopy with Aggregation-Induced Emission Dots. *Sci. Bull.* **2019**, *64* (6), 410−416.
(32) Le Jeannic, H.; Verma, V. B.; Cavaillès, A.; Marsili, F.; Shaw, M. D.; Huang, K.; Morin, O.; Nam, S. W.; Laurat, J. High-Efficiency WSi Superconducting Nanowire Single-Photon Detectors for Quantum State Engineering in the near Infrared. *Opt. Lett.* **2016**, *41* (22), 5341.
(33) Esmaeil Zadeh, I.; Los, J. W. N.; Gourgues, R. B. M.; Chang, J.; Elshaari, A. W.; Zichi, J. R.; Van Staaden, Y. J.; Swens, J. P. E.; Kalhor, N.; Guardiani, A.; Meng, Y.; Zou, K.; Dobrovolskiy, S.; Fognini, A. W.; Schaart, D. R.; Dalacu, D.; Poole, P. J.; Reimer, M. E.; Hu, X.; Pereira, S. F.; Zwiller, V.; Dorenbos, S. N. Efficient Single-Photon Detection with 7.7 Ps Time Resolution for Photon-Correlation Measurements. *ACS Photonics* **2020**, *7* (7), 1780−1787.
(34) Reddy, D. V.; Nerem, R. R.; Nam, S. W.; Mirin, R. P.; Verma, V. B. Superconducting Nanowire Single-Photon Detectors with 98% System Detection Efficiency at 1550 Nm. *Optica* **2020**, *7* (12), 1649.
(35) Hu, P.; Li, H.; You, L.; Wang, H.; Xiao, Y.; Huang, J.; Yang, X.; Zhang, W.; Wang, Z.; Xie, X. Detecting Single Infrared Photons toward Optimal System Detection Efficiency. *Opt. Express* **2020**, *28* (24), 36884−36891.
(36) Chang, J.; Los, J. W. N.; Tenorio-Pearl, J. O.; Noordzij, N.; Gourgues, R.; Guardiani, A.; Zichi, J. R.; Pereira, S. F.; Urbach, H. P.; Zwiller, V.; Dorenbos, S. N.; Esmaeil Zadeh, I. Detecting Telecom Single Photons with 99.5 - 2.07 + 0.5% System Detection Efficiency and High Time Resolution. *APL Photonics* **2021**, *6* (3), 036114.
(37) Marsili, F.; Bellei, F.; Najafi, F.; Dane, A. E.; Dauler, E. A.; Molnar, R. J.; Berggren, K. K. Efficient Single Photon Detection from 500 Nm to 5 μm Wavelength. *Nano Lett.* **2012**, *12* (9), 4799−4804.
(38) Chen, Q.; Ge, R.; Zhang, L.; Li, F.; Zhang, B.; Jin, F.; Han, H.; Dai, Y.; He, G.; Fei, Y.; Wang, X.; Wang, H.; Jia, X.; Zhao, Q.; Tu, X.; Kang, L.; Chen, J.; Wu, P. Mid-Infrared Single Photon Detector with Superconductor Mo0.8Si0.2 Nanowire. *Science Bulletin* **2021**, *66* (10), 965.
(39) Verma, V. B.; Korzh, B.; Walter, A. B.; Lita, A. E.; Briggs, R. M.; Colangelo, M.; Zhai, Y.; Wollman, E. E.; Beyer, A. D.; Allmaras, J. P. Single-Photon Detection in the Mid-Infrared up to 10 Micron Wavelength Using Tungsten Silicide Superconducting Nanowire Detectors. *arXiv:2012.09979 [physics.ins-det]* **2020**, na.
(40) Taylor, G. G.; Morozov, D.; Gemmell, N. R.; Erotokritou, K.; Miki, S.; Terai, H.; Hadfield, R. H. Photon Counting LIDAR at 2.3 μm Wavelength with Superconducting Nanowires. *Opt. Express* **2019**, *27* (26), 38147−38158.
(41) Xia, F.; Wu, C.; Sinefeld, D.; Li, B.; Qin, Y.; Xu, C. In Vivo Label-Free Confocal Imaging of the Deep Mouse Brain with Long-Wavelength Illumination. *Biomed. Opt. Express* **2018**, *9* (12), 6545.
(42) Liu, H.; Deng, X.; Tong, S.; He, C.; Cheng, H.; Zhuang, Z.; Gan, M.; Li, J.; Xie, W.; Qiu, P.; Wang, K. In Vivo Deep-Brain Structural and Hemodynamic Multiphoton Microscopy Enabled by Quantum Dots. *Nano Lett.* **2019**, *19* (8), 5260−5265.
(43) Theer, P.; Hasan, M. T.; Denk, W. Two-Photon Imaging to a Depth of 1000 μm in Living Brains by Use of a Ti: Al 2 O 3 Regenerative Amplifier. *Opt. Lett.* **2003**, *28* (12), 1022−1024.
(44) Wang, T.; Ouzounov, D. G.; Wu, C.; Horton, N. G.; Zhang, B.; Wu, C. H.; Zhang, Y.; Schnitzer, M. J.; Xu, C. Three-Photon Imaging of Mouse Brain Structure and Function through the Intact Skull. *Nat. Methods* **2018**, *15* (10), 789−792.
(45) Farsiu, S.; Christofferson, J.; Eriksson, B.; Milanfar, P.; Friedlander, B.; Shakouri, A.; Nowak, R. Statistical Detection and Imaging of Objects Hidden in Turbid Media Using Ballistic Photons. *Appl. Opt.* **2007**, *46* (23), 5805−5822.
(46) Wang, M.; Kim, M.; Xia, F.; Xu, C. Impact of the Emission Wavelengths on in Vivo Multiphoton Imaging of Mouse Brains. *Biomed. Opt. Express* **2019**, *10* (4), 1905.
(47) Smithpeter, C. L.; Dunn, A. K.; Welch, A. J.; Richards-Kortum, R. Penetration Depth Limits of in Vivo Confocal Reflectance Imaging. *Appl. Opt.* **1998**, *37* (13), 2749−2754.

https://doi.org/10.1021/acsphotonics.1c01018
ACS Photonics 2021, 8, 2800−2810

(48) Yang, M.-H.; Abashin, M.; Saisan, P. A.; Tian, P.; Ferri, C. G. L.; Devor, A.; Fainman, Y. Non-Degenerate 2-Photon Excitation in Scattering Medium for Fluorescence Microscopy. *Opt. Express* **2016**, *24* (26), 30173.
(49) Freudiger, C. W.; Min, W.; Saar, B. G.; Lu, S.; Holtom, G. R.; He, C.; Tsai, J. C.; Kang, J. X.; Xie, X. S. Christian W. Freudiger, Wei Min, Brian G. Saar, Label-Free Biomedical Imaging with High Sensitivity by Stimulated Raman Scattering Microscopy. *Science* **2008**, *322* (December), 1857−1861.
(50) Dong, P.-T.; Cheng, J.-X. Pump−Probe Microscopy: Theory, Instrumentation, and Applications. *Spectroscopy* **2017**, *32* (April), 2−11.
(51) Ju, K.-Y.; Degan, S.; Fischer, M. C.; Zhou, K. C. Unraveling the Molecular Nature of Melanin Changes in Metastatic Cancer. *J. Biomed. Opt.* **2019**, *24* (05), 1.
(52) Schmitt, J. M.; Ben-Letaief, K. Efficient Monte Carlo Simulation of Confocal Microscopy in Biological Tissue. *J. Opt. Soc. Am. A* **1996**, *13* (5), 952.
(53) Badon, A.; Li, D.; Lerosey, G.; Boccara, A. C.; Fink, M.; Aubry, A.; Boccara, C.; Fink, M.; Aubry, A. Smart Optical Coherence Tomography for Ultra-Deep Imaging through Highly Scattering Media. *Sci. Adv.* **2016**, *2* (11), No. e1600370.
(54) Theer, P.; Denk, W. On the Fundamental Imaging-Depth Limit in Two-Photon Microscopy. *J. Opt. Soc. Am. A* **2006**, *23* (12), 3139.
(55) Zhang, X.; Yin, X.; Zhang, J.; Li, A.; Gong, H.; Luo, Q.; Zhang, H.; Gao, Z.; Jiang, H. High-Resolution Mapping of Brain Vasculature and Its Impairment in the Hippocampus of Alzheimer's Disease Mice. *Natl. Sci. Rev.* **2019**, *6* (6), 1223−1238.
(56) Xie, C.; Schwen, L. O.; Wei, W.; Schenk, A.; Zafarnia, S.; Gremse, F.; Dahmen, U. Quantification of Hepatic Vascular and Parenchymal Regeneration in Mice. *PLoS One* **2016**, *11* (8), 1−19.
(57) Gigan, S. Optical Microscopy Aims Deep. *Nat. Photonics* **2017**, *11* (1), 14−16.
(58) Yoon, S.; Kim, M.; Jang, M.; Choi, Y.; Choi, W.; Kang, S.; Choi, W. Deep Optical Imaging within Complex Scattering Media. *Nat. Rev. Phys.* **2020**, *2* (3), 141−158.
(59) Zichi, J.; Chang, J.; Steinhauer, S.; von Fieandt, K.; Los, J. W. N.; Visser, G.; Kalhor, N.; Lettner, T.; Elshaari, A. W.; Zadeh, I. E.; Zwiller, V. Optimizing the Stoichiometry of Ultrathin NbTiN Films for High-Performance Superconducting Nanowire Single-Photon Detectors. *Opt. Express* **2019**, *27* (19), 26579.
(60) Esmaeil Zadeh, I.; Los, J. W. N.; Gourgues, R. B. M.; Steinmetz, V.; Bulgarini, G.; Dobrovolskiy, S. M.; Zwiller, V.; Dorenbos, S. N. Single-Photon Detectors Combining High Efficiency, High Detection Rates, and Ultra-High Timing Resolution. *APL Photonics* **2017**, *2* (11), 111301.
(61) Waggener, W. C. Absorbance of Liquid Water and Deuterium Oxide between 0.6 and 1.8 Microns: Comparison of Absorbance and Effect of Temperature. *Anal. Chem.* **1958**, *30* (9), 1569−1570.
(62) Wang, Y.; Wen, W.; Wang, K.; Zhai, P.; Qiu, P.; Wang, K. Measurement of Absorption Spectrum of Deuterium Oxide (D2O) and Its Application to Signal Enhancement in Multiphoton Microscopy at the 1700-Nm Window. *Appl. Phys. Lett.* **2016**, *108* (2), 021112.

NOTE ADDED AFTER ASAP PUBLICATION

This paper was published on September 2, 2021, with a misspelling in an author's name. The corrected version was reposted on September 2, 2021.

https://doi.org/10.1021/acsphotonics.1c01018
ACS Photonics 2021, 8, 2800−2810